Monthly Notices
of the
ROYAL ASTRONOMICAL SOCIETY

MNRAS **496,** 1554–1564 (2020)
Advance Access publication 2020 June 5

doi:10.1093/mnras/staa1581

Deep *XMM–Newton* observations of the most distant SPT-SZ galaxy cluster

Adam B. Mantz [1,2]‹ Steven W. Allen,[1,2,3] R. Glenn Morris,[1,2,3] Rebecca E. A. Canning,[1,2] Matthew Bayliss,[4] Lindsey E. Bleem,[5,6] Benjamin T. Floyd[7] and Michael McDonald[8]

[1]*Kavli Institute for Particle Astrophysics and Cosmology, Stanford University, 452 Lomita Mall, Stanford, CA 94305, USA*
[2]*Department of Physics, Stanford University, 382 Via Pueblo Mall, Stanford, CA 94305, USA*
[3]*SLAC National Accelerator Laboratory, 2575 Sand Hill Road, Menlo Park, CA 94025, USA*
[4]*Department of Physics, University of Cincinnati, Cincinnati, OH 45221, USA*
[5]*HEP Division, Argonne National Laboratory, Argonne, IL 60439, USA*
[6]*Kavli Institute for Cosmological Physics, University of Chicago, Chicago, IL 60637, USA*
[7]*Department of Physics and Astronomy, University of Missouri, 5110 Rockhill Road, Kansas City, MO 64110, USA*
[8]*Kavli Institute for Astrophysics and Space Research, Massachusetts Institute of Technology, 77 Massachusetts Avenue, Cambridge, MA 02139, USA*

Accepted 2020 May 30. Received 2020 May 29; in original form 2020 April 22

ABSTRACT

We present results from a 577 ks *XMM–Newton* observation of SPT-CL J0459–4947, the most distant cluster detected in the South Pole Telescope 2500 square degree (SPT-SZ) survey, and currently the most distant cluster discovered through its Sunyaev–Zel'dovich effect. The data confirm the cluster's high redshift, $z = 1.71 \pm 0.02$, in agreement with earlier, less precise optical/IR photometric estimates. From the gas density profile, we estimate a characteristic mass of $M_{500} = (1{\cdot}8 \pm 0{\cdot}2) \times 10^{14}\,\mathrm{M}_\odot$; cluster emission is detected above the background to a radius of $\sim 2{\cdot}2\,r_{500}$, or approximately the virial radius. The intracluster gas is characterized by an emission-weighted average temperature of 7.2 ± 0.3 keV and metallicity with respect to Solar of $Z/Z_\odot = 0{\cdot}37 \pm 0{\cdot}08$. For the first time at such high redshift, this deep data set provides a measurement of metallicity outside the cluster centre; at radii $r > 0{\cdot}3\,r_{500}$, we find $Z/Z_\odot = 0{\cdot}33 \pm 0{\cdot}17$ in good agreement with precise measurements at similar radii in the most nearby clusters, supporting an early enrichment scenario in which the bulk of the cluster gas is enriched to a universal metallicity prior to cluster formation, with little to no evolution thereafter. The leverage provided by the high redshift of this cluster tightens by a factor of 2 constraints on evolving metallicity models, when combined with previous measurements at lower redshifts.

Key words: galaxies: clusters: individual: SPT-CL J0459–4947 – galaxies: clusters: intracluster medium – X-rays: galaxies: clusters.

1 INTRODUCTION

Over the past three decades, sky surveys have progressively extended the discovery space for clusters of galaxies in the Universe. At present, surveys at X-ray, optical/IR, and mm wavelengths, respectively, sensitive to bremsstrahlung emission from the intracluster medium (ICM), galaxy light, and the Sunyaev–Zel'dovich (SZ) effect of the ICM have together revealed thousands of massive clusters out to a redshift of $z \sim 2$ (e.g. Ebeling et al. 2000; Ebeling, Edge & Henry 2001; Böhringer et al. 2004; Rykoff et al. 2012; Hasselfield et al. 2013; Willis et al. 2013; Bleem et al. 2015; Planck Collaboration 2016; Adami et al. 2018; Gonzalez et al. 2019). Though still less numerous than those at $z < 1$, cluster discoveries at high redshifts are now routine. The next generation of surveys is poised to extend these searches to redshifts of 3–4, into the epoch where massive, virialized systems first formed.

While the population of massive clusters has now been extensively characterized at $z \lesssim 0{\cdot}5$ (e.g. Allen, Evrard & Mantz 2011; Giodini et al. 2013), with multiwavelength data sets becoming increasingly complete out to $z \sim 1$–1.5, few detailed studies have been performed at the highest redshifts now available, $1{\cdot}5 \lesssim z \lesssim 2$ (e.g. Gobat et al. 2011, 2019; Andreon et al. 2014; Mantz et al. 2014, 2018; Brodwin et al. 2016; Willis et al. 2020). Known systems in this range represent a mix of genuinely virialized clusters and forming protoclusters, and, due to their large distances, remain challenging to observe. Nevertheless, characterizing this population is a key

E-mail: amantz@stanford.edu

Table 1. Clean exposure times after automatic and manual filtering for each of the *XMM* (MOS1, MOS2, and PN) and *Chandra* (ACIS-I) detectors used in this work.

OBSID	MOS1	MOS2	PN	OBSID	ACIS-I
0801950101	101	103	89	17211	13
0801950201	97	96	85	17501	22
0801950301	95	95	82	17502	14
0801950401	67	66	52	18711	23
0801950501	18	19	14	18824	22
				18853	30
Total (ks)	378	379	321		123

step towards extending our understanding of cluster physics and evolution into the epoch where they first form.

Key questions that observations of these high-redshift clusters can address include the mechanism by which the ICM is enriched with metals, and the impact of non-gravitational processes on the ICM thermodynamics. The deep potential wells of clusters mean that the ICM retains most of the metals produced by stars in cluster member galaxies. Observations over the last decade have revealed a universal and spatially uniform enrichment of the ICM in low-redshift clusters (e.g. Werner et al. 2013; Simionescu et al. 2015, 2017). This implies early enrichment to a constant level in the protocluster intergalactic medium, prior to cluster formation, at $z \gtrsim 2$, and makes the firm prediction that clusters at redshifts 1.5–2 should have similar metal abundances to nearby clusters.

In this work, we have targeted the highest redshift cluster discovered in the South Pole Telescope (SPT) 2500 square degree SZ survey with detection significance > 5, SPT-CL J0459–4947 (henceforth SPT J0459). The original SPT-SZ cluster catalogue contained three clusters whose redshifts were conservatively reported as $z > 1.5$, since the available ground-based optical and *Spitzer* IR photometric data could not provide a precise redshift estimate beyond this limit (Bleem et al. 2015). Of these, SPT J0459 has the highest SZ detection significance and is thus presumably the most massive. Of the others, SPT-CL J0446–4606 now has a revised photometric redshift of $1{\cdot}52^{+0{\cdot}13}_{-0{\cdot}02}$ from *Hubble* and *Spitzer* data (Strazzullo et al. 2019), while SPT-CL J0334–4645 was detected with survey significance < 5 and therefore not prioritized for confirmation (nor used in e.g. cosmological analyses; de Haan et al. 2016). SPT J0459 is thus the highest redshift confirmed cluster found by SPT-SZ, and, at this writing, is the highest redshift cluster originally discovered through its SZ effect. With the results reported here, it joins a small group of confirmed, massive clusters at $z > 1.7$, the others having all been discovered using X-ray or IR data.

Chandra observations of SPT J0459 were able to measure the cluster's X-ray luminosity and ICM density (McDonald et al. 2017). Based on its known flux, we designed an *XMM–Newton* observing programme aimed at resolving the metallicity and temperature structure of the cluster in multiple radial ranges, a first for such a high redshift. While exceedingly modest compared with studies that have routinely been done at low redshift, these goals required several hundred ks of observing time, even with *XMM*'s high throughput. We describe the reduction of these data, along with the archival *Chandra* data, in Section 2. Section 3 covers our modelling of the ICM and contaminating point sources, as well as the *XMM* point spread function (PSF), which must be accounted for to study this distant, compact source. Our results and their implications are presented in Sections 4 and 5. We conclude in Section 6.

All cosmology-dependent quantities reported in this work were computed for a reference flat, cosmological-constant model with Hubble parameter 70 km s^{-1} Mpc^{-1} and matter density with respect to the critical density $_m = 0.3$. Parameter values correspond to marginalized posterior modes, and quoted uncertainties to 68.3 per cent highest posterior density credible intervals. The characteristic mass and radius of a cluster are jointly defined by the relation $M = (4/3)\pi \rho_{cr}(z) r^3$, where $\rho_{cr}(z)$ is the critical density at the cluster's redshift and $= 500$.

2 DATA REDUCTION

2.1 *XMM–Newton*

SPT J0459 was observed by *XMM* for a total of 577 ks (before filtering) between 2017 April and November (Table 1). These data were reduced using the *XMM–Newton* Extended Source Analysis Software (XMM-ESAS; SAS version 18.0.0),[1] following the recommendations of Snowden et al. (2008) and the XMM-ESAS Cookbook.[2] Following standard calibration and filtering of the raw event files, light curves for each of the EPIC detectors were manually inspected, and periods in which the X-ray background was enhanced (flared) were manually removed. The clean exposure times for the MOS (PN) detectors, after accounting for overheads and light-curve filtering, were 56 (66) per cent of the total, in line with historical expectations (Salvetti et al. 2017). The final clean exposure times for the PN, MOS1, and MOS2 are, respectively, 378, 379, and 321 ks. From these event files, we produced images, quiescent background maps, and exposure maps corresponding to 0.4–4.0 keV observer-frame energies for our imaging analysis (Section 3.2), as well as spectra, response matrices, and ancillary response files for our later spectral analysis.

2.2 *Chandra*

We use archival *Chandra* observations of SPT J0459, totaling 139 ks (see McDonald et al. 2017). The data were processed as described by Mantz et al. (2015), with the exception that this work employs a more recent version of the *Chandra* calibration files (specifically, CALDB[3] version 4.7.1). In brief, the raw data were reprocessed to produce level 2 event files, and were filtered to eliminate periods of high background. The total clean exposure time after this step was 123 ks. For each observation, a corresponding quiescent background data set was produced using the *Chandra* blank-sky data[4], rescaled according to the measured count rate in the 9.5–12 keV band. Our pipeline produces images, blank-sky background maps and exposure maps in the 0.6–2.0 keV band.

3 MODELLING

3.1 Point-like sources

A preliminary catalogue of active galactic nuclei (AGNs) detected in the *Chandra* data by the Cluster AGN Topography Survey pipeline (CATS; Canning et al. in preparation) was used to produce a mask for the *Chandra* and *XMM* data. In the case of *XMM*, the measured

[1] http://www.cosmos.esa.int/web/xmm-newton/sas
[2] http://heasarc.gsfc.nasa.gov/docs/xmm/esas/cookbook/
[3] http://cxc.harvard.edu/caldb/
[4] http://cxc.cfa.harvard.edu/ciao/threads/acisbackground/

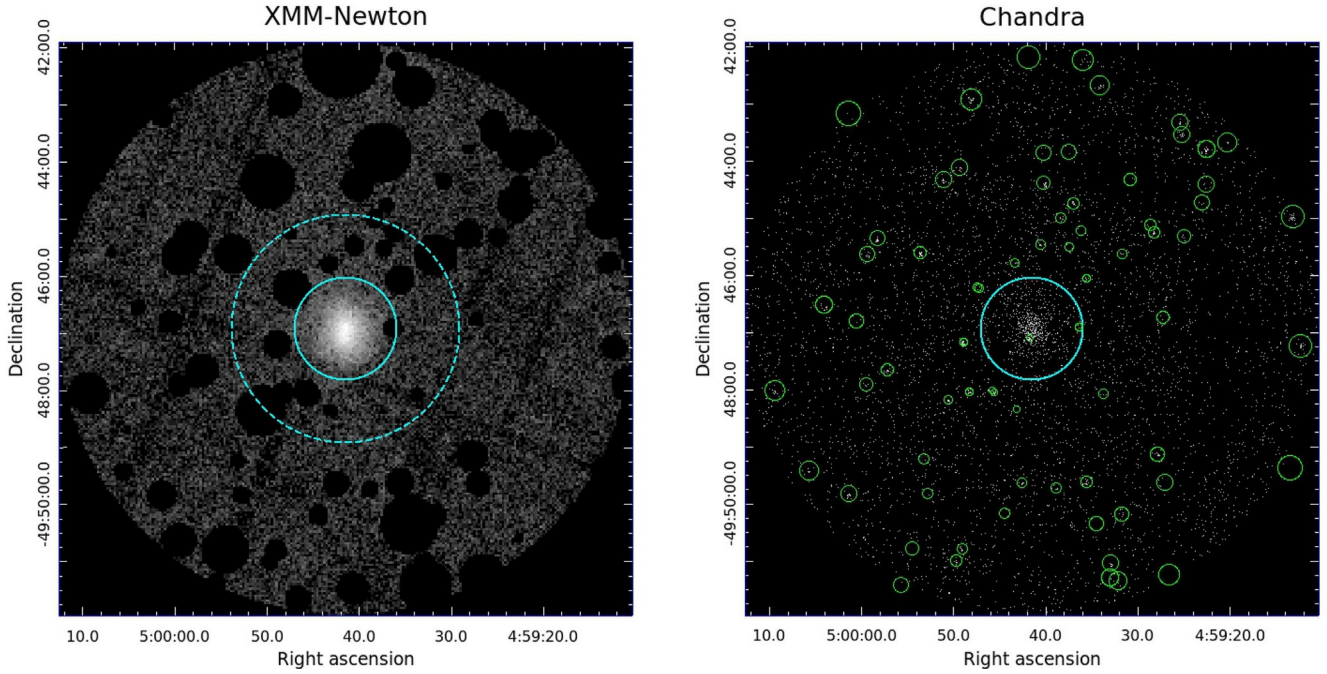

Figure 1. Stacked images from the *XMM* and *Chandra* observations of SPT J0459. The solid cyan circle shows our estimate of $r_{500} \approx 54$ arcsec (Section 4.2), while the dashed cyan circle approximately corresponds to the detected extent of the cluster emission (radius 2 arcmin; Section 3.2). Point-like sources identified in the *Chandra* data are circled in green in the right-hand panel (Section 3.1).

CATS flux of each AGN was used to resize the corresponding circular mask, such that the maximum surface brightness *not* covered by the mask was 5×10^{-19} erg s^{-1} cm^{-2} arcsec^{-2} in the 0.4–4 keV band used in our image analysis below; this calculation used the *XMM* PSF model described in the next section. A maximum radius of 60 arcsec was enforced in this process, though it was never realized within the 5 arcmin radius region used in our analysis throughout this work. While these particular choices were made to produce visually reasonable masks, we note that the residual, unmasked brightness is significantly less than the residual background level found in the next section. The one exception to this process is for a relatively faint AGN appearing within the bulk of the cluster emission (2–10 keV flux of 4.3×10^{-15} erg s^{-1} cm^{-2}, projected 11 arcsec from the cluster centre) which cannot practically be masked in the same way. Instead, the contaminating flux from this source is forward modelled in our spectral analysis (Section 3.4), assuming a power-law spectrum with index -1.4; the source is faint enough that assuming a steeper index or even neglecting it entirely has a $<1\sigma$ impact on our spectral results. In addition, a small number of variable sources that are visible in the *XMM* but not the *Chandra* data were masked manually. The stacked *XMM* and *Chandra* images, respectively, showing the mask and the detected point sources, appear in Fig. 1. The final mask used in the *XMM* analysis removes 20 per cent of the area in the central 5 arcmin radius circle.

3.2 *XMM–Newton* PSF

The high redshift of SPT J0459 means that our analysis can be confined to the central portion of the FoV and to relatively low energies (<4 keV). We therefore adopt a model for the *XMM* PSF that is axisymmetric and monochromatic, consisting of the sum of a Gaussian 'core' and a more extended β profile (Read et al. 2011), and apply it to each EPIC detector. As a sanity check, we extract surface brightness profiles from the *XMM* and *Chandra* data about a common centre, converting these to intensity units (erg s^{-1} cm^{-2} arcsec^{-2}) using PIMMS,[5,6] assuming a fiducial temperature of 7 keV, a metallicity of $0.3\,Z$ and a redshift of 1.7, and accounting for Galactic absorption (see Section 3.3). We fit a β model plus constant residual background to each data set independently, excluding the point source masks described in the previous section. For *Chandra*, we use the 'blank sky' data sets (rescaled to account for relative exposure times) from standard data reduction, which in principle contain all astrophysical and instrumental backgrounds. The model is scaled by the exposure map, added to the blank sky image, and compared to the measured counts in the science image using the Cash (1979) statistic (i.e. using a Poisson likelihood function). We used the RGW[7] Markov Chain Monte Carlo (MCMC) code to obtain constrains on the model parameters. For *XMM*, the procedure is slightly different. We use the model quiescent particle background maps generated by SAS, which represent only a fraction of the total background, in lieu of 'blank sky' images; hence the constant background model parameter fits to a positive value in this case rather than being consistent with zero. More importantly, the β model is convolved with the PSF before being compared with the data. Fig. 2 shows that the cluster model, fit to the *XMM* data in this way, is consistent with the higher resolution *Chandra* surface brightness profile. Conversely, the model fit to the *Chandra* data, if convolved with the *XMM* PSF model, matches the *XMM* profile well. We have checked that the same conclusions hold when using *XMM* images in separate soft and (relatively) hard energy bands (0.4–1.5 and 1.5–4.0 keV).

[5] https://heasarc.gsfc.nasa.gov/cgi-bin/Tools/w3pimms/w3pimms.pl
[6] http://cxc.harvard.edu/toolkit/pimms.jsp
[7] https://github.com/abmantz/rgw

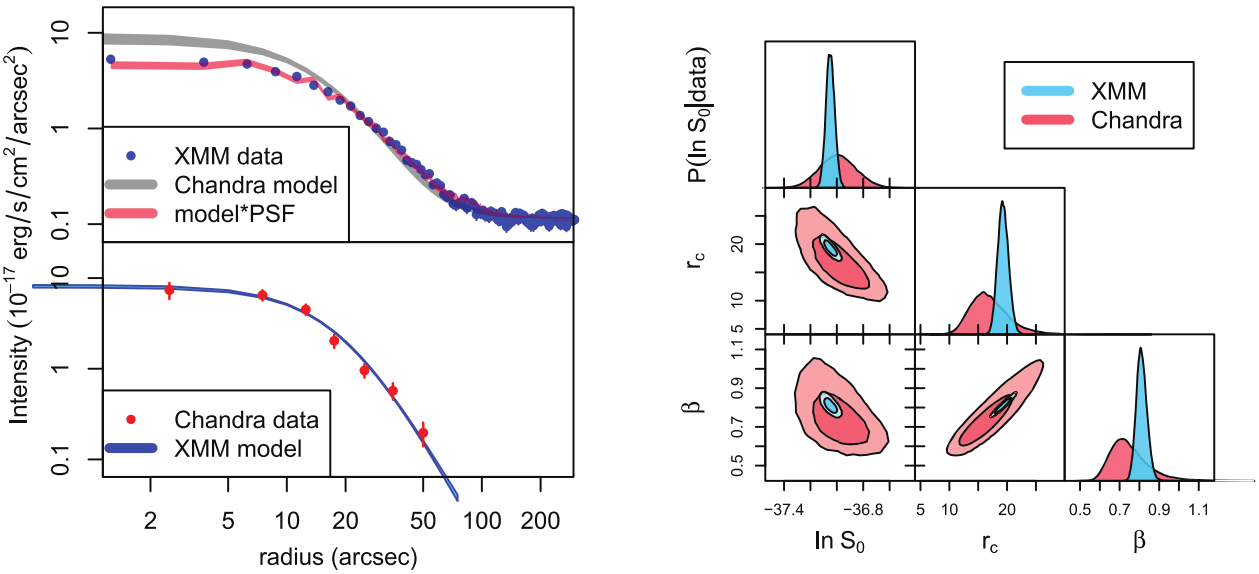

Figure 2. Left: Intensity profiles of SPT J0459 in the 0.4–4.0 keV band from *XMM* and *Chandra* data. Profiles are binned for display, although our analysis runs on profiles made at pixel resolution. A β model plus constant background is fit to each data set independently. In the upper panel, the *XMM* data are compared with the sum of the β model fitted to the *Chandra* data and the constant background fitted to the *XMM* data (grey shading). The red shading shows this model after being convolved with the *XMM* PSF. Conversely, the bottom panel compares the *Chandra* profile with the sum of the β model from the *XMM* fit (accounting for the PSF) and the residual *Chandra* background fit. Right: One-dimensional (on-diagonal) and two-dimensional (off-diagonal) marginalized posteriors of the β model parameters from *XMM* (blue) and *Chandra* (red). Here, S_0 has units of erg s^{-1} cm^{-2} arcsec^{-2} and r_c has units of arcsec. See Section 3.2.

This agreement gives us confidence that the simple PSF model employed here is adequate for our analysis below.

In the *XMM* surface brightness profile, cluster emission can be seen (that is, the net enclosed counts in excess of the background are clearly increasing) out to a radius of ~ 2 arcmin. This is a factor of 2.2 times the estimate of r_{500} we arrive at in Section 4.2, meaning that the cluster is visible to approximately the virial radius. This is due to both the depth of our data, the relatively higher physical density at the virial radius at high redshifts compared with low redshifts, and (to a lesser extent) the large angular diameter distance to the cluster leading to an increased surface brightness. By comparison, XLSSC 122, a fainter cluster at $z = 1.98$, was detected to approximately $r_{200} \approx 1{\cdot}5\, r_{500}$ in 100 ks of *XMM* observation (Mantz et al. 2018).

3.3 Intracluster medium

We adopt (4:59:41.4,−49:46:56; J2000 coordinates), the median photon position in the *Chandra* image after masking point sources (Mantz et al. 2015), as the cluster centre. This is within 1 arcsec of the bright central galaxy position, and is preferable to using a centre determined from the *XMM* data due to the presence of a faint point source within the bright part of the cluster (Section 3.1). With the exception of the 'single spectrum' results in Section 4.1, our analysis seeks to determine properties of the ICM as a function of radius in three dimensions. In these cases, spectra are therefore extracted in at least two concentric annuli. The cluster model consists of emission from a series of concentric spherical shells, with inner and outer three-dimensional radii corresponding to the projected radii of the annuli within which spectra are extracted. However, a given annulus potentially contains signal from every spherical shell for two reasons. First, the emission from each shell is geometrically projected on to all annuli at equal or smaller radius. Secondly, the PSF spreads photons originating at a given position on the sky across all annuli at some level. For a given set of annuli/shells, we compute the overall mixing matrix, encoding the fraction of emission from each shell ending up in each annulus. Within this calculation, we use the best-fitting β model fit to the *XMM* data (converted to a three-dimensional emissivity profile, when considering the mixing due to geometric projection) as a template for the radial dependence of emissivity within each shell/annulus. Note that this aspect differs from the geometric projection model PROJCT in XSPEC, which assumes a constant emissivity within each shell, and also from the use of 'cross-talk' ancillary response files to model PSF mixing. Given the prior that the cluster emission resembles a β model, which in this case is directly verifiable using the higher resolution *Chandra* data, our approach should result in a more accurate model of the mixing between the cluster centre and the outskirts.

3.4 Spectral analysis details

Our spectral analysis uses XSPEC[8] (version 12.10) to compute spectral models and evaluate likelihoods, and the LMC MCMC code[9] to estimate parameter posterior distributions. Bremsstrahlung continuum and line emission from the ICM were evaluated using the APEC plasma model (ATOMDB version 3.0.9), parametrized by a temperature, metallicity (with relative abundances of different metals fixed to the Solar ratios of Asplund et al. 2009), redshift, and overall normalization. Photoelectric absorption by Galactic gas was accounted for using thePHABS model, employing the cross-sections of Balucinska-Church & McCammon (1992), and adopting a fixed value of $1{\cdot}19 \times 10^{20}$ cm^{-2} for the equivalent absorbing hydrogen column density (Kalberla et al. 2005); updating this to the more recent value of $1{\cdot}08 \times 10^{20}$ cm^{-2} (HI4PI Collaboration 2016) has a

[8] http://heasarc.gsfc.nasa.gov/docs/xanadu/xspec/
[9] https://github.com/abmantz/lmc

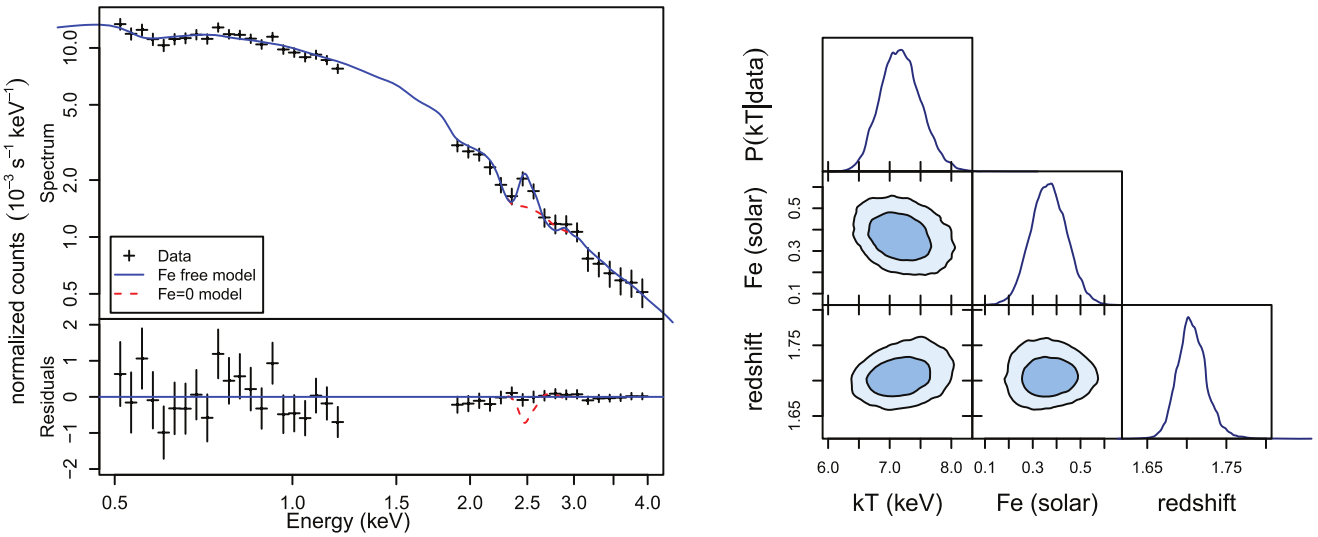

Figure 3. Left: Stacked and background-subtracted (for display only) EPIC spectrum of the central arcminute of SPT J0459. Energies in the 1.2–1.9 keV range are excluded due to contamination from instrumental emission lines. The blue, solid curve shows the best-fitting single thermal component model, with a free temperature, metallicity, redshift, and normalization. The red, dashed curve shows the best-fitting model, where the metallicity is fixed to zero, to indicate the strength of the Fe emission feature. The lower panel shows residuals with respect to the model with fitted metallicity. Right: one-dimensional (on-diagonal) and two-dimensional (off-diagonal) marginalized posteriors for the cluster emission model fit to these data.

Table 2. Measured temperatures and metallicities of SPT J0459, marginalized over the cluster redshift in all cases. Shown are results from a single spectrum; two concentric annuli, where mixing of emission from the PSF is accounted for but geometric projection is not; and the same annuli when both the PSF and projection are accounted for. Net (background subtracted) counts are in the 0.5–4.0 keV band. The final column compares the best C statistic with the number of degrees of freedom.

Deprojected	$r^{(1)}_{\rm inner}$ (arcsec)	$r^{(1)}_{\rm outer}$ (arcsec)	$kT^{(1)}$ (keV)	$Z^{(1)}$ ($Z_\odot$)	$r^{(2)}_{\rm inner}$ (arcsec)	$r^{(2)}_{\rm outer}$ (arcsec)	$kT^{(2)}$ (keV)	$Z^{(2)}$ ($Z_\odot$)	Net counts	cstat/dof
No	0	60	7.2 ± 0.3	0.37 ± 0.08	–	–	–	–	11 499	4351/5121
No	0	16	8.3 ± 0.7	0.52 ± 0.15	16	120	$6{\cdot}1^{+0{\cdot}9}_{-0{\cdot}7}$	0.29 ± 0.18	12 704	8109/8998
Yes	0	16	10.3 ± 2.3	0.69 ± 0.35	16	120	$5{\cdot}9^{+0{\cdot}9}_{-0{\cdot}6}$	0.33 ± 0.17	12 704	8109/8998

negligible impact on our results. As mentioned in Section 3.1, we model the contribution from a single AGN identified in the *Chandra* data but not masked. We model the remaining astrophysical and instrumental backgrounds empirically using a spectrum extracted from an annulus spanning radii 3–5 arcmin from the cluster centre. Our surface brightness model from Section 3.2 indicates that the cluster signal at 3 arcmin is $\lesssim$ 1 per cent of the background, and the cluster flux expected to be mixed from the background region to radii $<$ 2 arcmin (the greatest extent of our cluster analysis below) is correspondingly negligible. The model parameters are fit using the Cash (1979) statistic, as modified for XSPEC by Arnaud (1996, the C statistic), to properly account for the Poisson nature of the source and background counts. Spectra were binned to have at $\geq$ 1 count per channel, as the modified C statistic is known to be biased when the data include empty channels. [10] We fit data in the observer-frame energy band 0.5–4.0 keV (rest-frame energies $\sim$ 1.4–11 keV), with the exception of the ranges 1.2–1.9 keV (for MOS) and 1.2–1.65 keV (for PN), which are heavily contaminated by aluminium and (in MOS) silicon instrumental emission lines.

[10] XSPEC manual Appendix B: https://heasarc.gsfc.nasa.gov/docs/xanadu/xspec/manual/node304.html.

4 RESULTS

4.1 Single spectrum

We first fit *XMM* spectra extracted from a single circular region of radius 1 arcmin about the cluster centre. While detectable emission from the cluster extends to $\sim$ 2 arcmin radius, this smaller region contains $>$ 90 per cent of the total cluster signal; the radius of 1 arcmin is also conveniently very close to the estimate of $r_{500} \approx 54$ arcsec derived in the next section. From these data, we constrain the 'average' properties of the ICM to be $kT = 7.2 \pm 0.3$, $Z/Z_\odot = 0{\cdot}37 \pm 0{\cdot}08$ and $z = 1.705 \pm 0.018$. Our redshift constraint, due to the (rest frame) 6.7 keV Fe emission line complex, is consistent with earlier photometric estimates of 1.7 ± 0.2 (*Spitzer* IR and ground-based NIR data; Bleem et al. 2015) and $1{\cdot}80^{+0{\cdot}10}_{-0{\cdot}19}$ (*Spitzer* and *Hubble* imaging; Strazzullo et al. 2019). Fig. 3 shows the stacked *XMM* EPIC spectra used in this fit, and the corresponding parameter constraints (see also Table 2). Note that we continue to marginalize over the cluster redshift in the spectral fits below, rather than fixing it based on these results.

4.2 Density deprojection

To constrain the ICM density profile, we fit spectra extracted in annuli whose outer radii correspond to the points shown in the

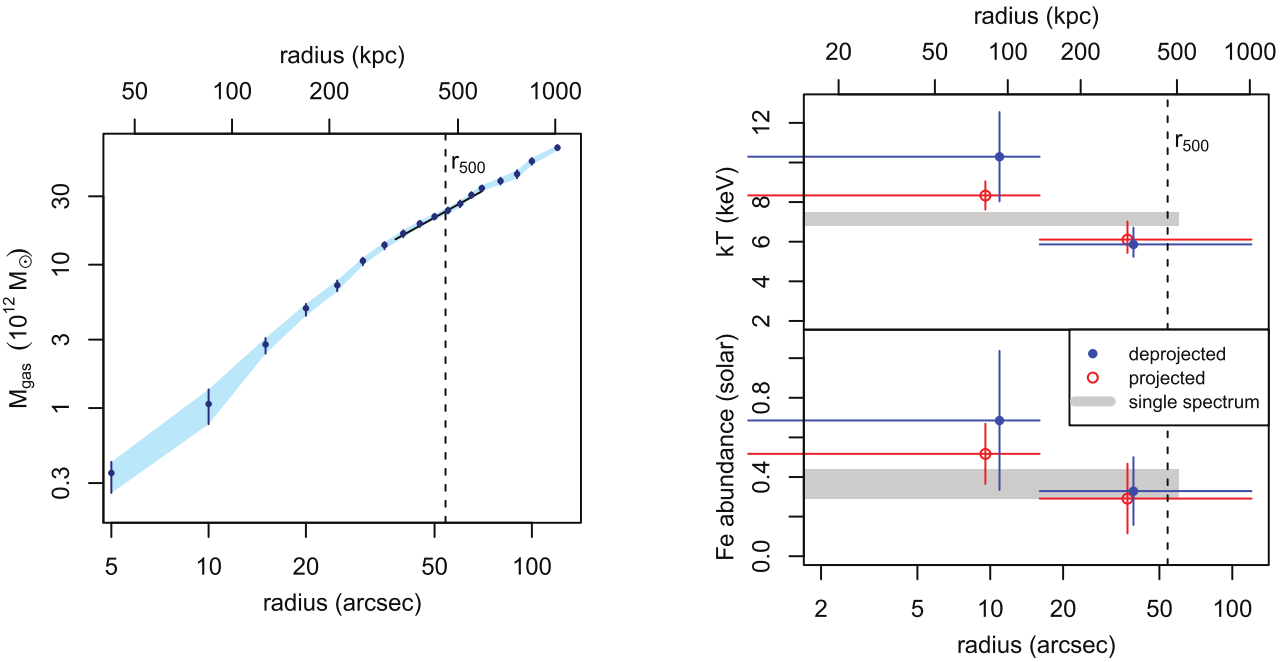

Figure 4. Left: Enclosed gas mass profile of SPT J0459 as determined from our analysis in Section 4.2. While the spectral fit leading to this profile marginalizes over cluster redshift, the values of gas mass and radius in physical units shown here assume a cluster redshift of $z = 1.71$. Error bars and shading indicate the 68.3 per cent confidence intervals as a function of radius. The vertical, dashed line shows our estimate of r_{500}, which is insensitive to the assumed redshift within the posterior redshift uncertainty. The solid line shows the typical power-law slope of the gas mas profile at $\sim r_{500}$, 1.25, measured from $z < 0.5$ clusters (Mantz et al. 2016b), with which the measured profile of SPT J0459 agrees well. Right: Constraints on temperature and metallicity from the single-spectrum analysis of Section 4.1, as well as the two-annulus analysis of Section 4.3. Blue points show the results obtained from our standard analysis, accounting for mixing due to both the PSF and geometrical projection (i.e. the values correspond to spherical shells of gas). For comparison, red points show the results when geometrical projection is not accounted for, corresponding instead to the projected properties of the two annuli. Points are shown at the emission-weighted average radius associated with each measurement, either in projection or in three dimensions.

left-hand panel of Fig. 4. The largest radius included in the cluster model is 2 arcmin, corresponding to a signal-to-background ratio of ~ 0.05, according to the surface brightness model of Section 3.2. Using the methods described in Section 3, we fit for the emissivity in each of the corresponding spherical shells, as well as a common temperature, metallicity and redshift. Fig. 4 shows the resulting constraints on the integrated gas mass profile, where we have assumed a canonical value of the mean molecular mass of $\mu = 0.61 m_{\rm p}$ and a cluster redshift of $z = 1.71$ when converting emissivity to gas density, and ultimately to gas mass, and angular separation to metric radius.

We arrive at an estimate of M_{500}, and the corresponding radius r_{500}, by solving the implicit equation

$$M(r_{500}) = \frac{M_{\rm gas}(r_{500})}{f_{\rm gas}(r_{500})} = \frac{4\pi}{3} 500 \rho_{\rm cr}(z) r_{500}^3. \quad (1)$$

For this purpose, we adopt a fiducial value of $f_{\rm gas}(r_{500}) = 0.125$, based on results from massive, X-ray selected clusters at $z < 0.5$ (Mantz et al. 2016b), and also consistent with dynamically relaxed clusters at redshifts $z < 1.08$ (Mantz et al. 2016a). While this value of $f_{\rm gas}(r_{500})$ has not been independently verified to apply at $z \sim 1.7$, the gas mass fraction is theoretically expected to be non-evolving at intermediate radii for massive clusters (e.g. Eke, Navarro & Frenk 1998; Nagai, Vikhlinin & Kravtsov 2007; Battaglia et al. 2013; Planelles et al. 2013; Barnes et al. 2017; Singh et al. 2020). This is supported by the good agreement between the slope of the $M_{\rm gas}(r)$ profile at these radii and the average value for the cluster sample of Mantz et al. (2016b), shown in Fig. 4. This procedure yields a characteristic radius of $r_{500} = (458 \pm 18)$ kpc (54 arcsec $\pm$ 2 arcsec) and mass of $M_{500} = (1{\cdot}8 \pm 0{\cdot}2) \times 10^{14}\,{\rm M}_\odot$, when using a cluster redshift of $z = 1.71$ in the unit conversions discussed above; this marginally lower than the mass of $(2{\cdot}7 \pm 0{\cdot}6) \times 10^{14}\,M_\odot$ estimated from the SZ signal by Bleem et al. (2015). Accounting for the posterior uncertainty on the cluster redshift in these computations has a negligible impact, at the < 1 per cent level for r_{500} (as expressed in kpc).

4.3 Temperature and metallicity deprojection

To move beyond a single free temperature and metallicity for the ICM, we simplify the analysis to spectra extracted within two annuli, rather than the large number of annuli used in Section 4.2. This minimizes the impact of binning each spectrum to ≥ 1 count per channel, and the corresponding loss of energy resolution, on fitting the Fe emission feature. Table 2 and the right-hand panel of Fig. 4 show the temperature and metallicity profile constraints at radii of 0–16 arcsec and 16 arcsec to 2 arcmin, corresponding to 0.0–0.3 r_{500} and 0.3–2.2 r_{500}. In addition to these 'deprojected' results, showing constraints on these quantities in spherical shells, the figure compares to constraints where the PSF, but not geometrical projection, is accounted for, as well as the single-spectrum results from Section 4.1. Points in the right-hand panel of Fig. 4 are located at the emission-weighted average radius associated with each annulus or shell, approximately reflecting which radii are most influential in the fit. Fig. 5 shows the spectra of the two annuli, along with constraints on the parameters of interest.

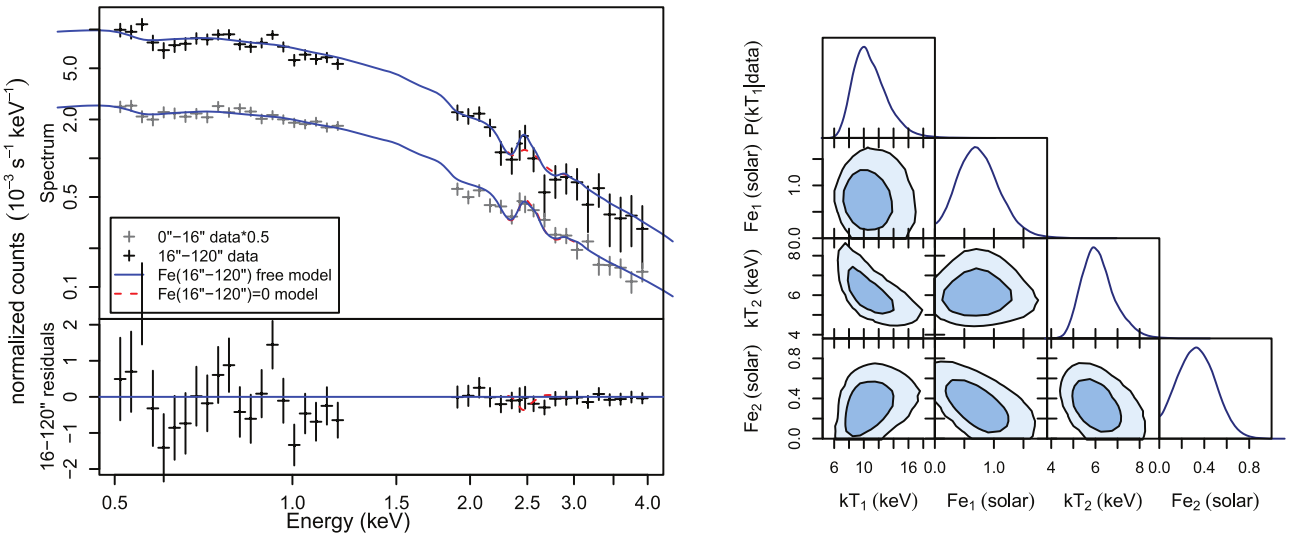

Figure 5. As Fig. 3, but for the deprojection analysis in Section 4.3, showing the posteriors for the temperature and metallicity of two spherical shells. The cluster redshift is marginalized over, although we do not include it in the right-hand panel; constraints are similar to those in Fig. 3. The 'Fe = 0' and 'Fe free' models in the left-hand panel refer to the metallicity in the outer shell. The metallicity of the inner shell is free in both cases, and PSF mixing thus produces an emission line feature in the outer annulus even for the 'Fe = 0' case. The data and models for the inner annulus are scaled by a factor of 0.5 in the left-hand panel for clarity.

5 DISCUSSION

5.1 ICM metallicity evolution

Multiple lines of evidence point to a uniform and universal enrichment of the intergalactic medium with the products of stellar evolution at high redshifts ($z \gtrsim 2$) and prior to the formation of massive clusters of galaxies. In the brightest, nearby clusters, where abundances of Fe and other heavy elements can be measured with high spatial resolution (in metric units) and signal-to-noise ratio, spatially uniform metal distributions have been observed outside of cluster cores, extending even to their virial radii (Werner et al. 2013; Simionescu et al. 2015, 2017). Azimuthally averaged metallicity profiles have shown a central peak, whose magnitude depends on the presence or absence of a cool core, declining to a universal value ($\sim 0.3Z$ for Fe) at larger radii (e.g. Allen & Fabian 1998; De Grandi et al. 2004; Leccardi & Molendi 2008; Thölken et al. 2016; Mernier et al. 2017; Urban et al. 2017; Urdampilleta et al. 2019). Studies of the evolution of the ICM metallicity have produced a variety of conclusions, partly due to differences in the radial ranges probed by different observations (e.g. Balestra et al. 2007; Leccardi & Molendi 2008; Maughan et al. 2008; Anderson et al. 2009; Andreon 2012; Baldi et al. 2012; Ettori et al. 2015; McDonald et al. 2016; Mantz et al. 2017). The picture that emerges is one where the gas that forms the ICM was pre-enriched and well mixed to a universal level prior to the formation of a deep potential well, with stellar evolution, galactic winds, and redistribution of gas by AGN feedback continuing to slowly enrich and mix the ICM near cluster centres, while the universal metallicity value is retained at larger radii. Simulations support this notion, finding that AGN feedback at $z \gtrsim 2$, when cluster potentials are still relatively shallow, is particularly effective at mixing metals throughout the ICM, producing similar radial trends to those observed, and minimal evolution (Fabjan et al. 2010; Biffi et al. 2017).

Although the available data are consistent with this early enrichment scenario, constraints on the evolution of the centre-excluded ICM metallicity are still relatively weak. The only results to date that both exclude cluster centres (out to 10s of per cent of r_{500}) and extend to redshifts $z > 1$ are those of Ettori et al. (2015) and Mantz et al. (2017), respectively, based on *XMM* and *Chandra* + *Suzaku* data. For models where the metallicity at large radii evolves as $(1+z)^{\gamma}$, these authors, respectively, find $\gamma = -0.26 \pm 0.61$ and $\gamma = 0.35^{+1.18}_{-0.36}$ from cluster samples spanning redshifts 0.09–1.4 and 0.02–1.03. What principally limits these constraints is both the lack of data at very high redshifts, and the relatively low statistical power of the observations that do exist at $z \gtrsim 1$. The results presented in Section 4.3 represent the first constraint on the centre-excluded metallicity in such a high-redshift cluster, and thus can provide significant leverage on its evolution. In particular, we find a metallicity of $Z/Z = 0.33 \pm 0.17$ at radii of 0.3–2.2 r_{500}.

Note that the outer annulus adopted in this analysis extends to somewhat smaller radii than were used in the works cited above, $r > 0.3\,r_{500}$ as compared with $> 0.4\,r_{500}$ (Ettori et al. 2015) and 0.5–1.0 r_{500} (Mantz et al. 2017). This is motivated by the observation of Mantz et al. (2017) that the metallicity in the intermediate radial range of 0.1–0.5 r_{500} is consistent with a constant at redshifts $z \gtrsim 0.4$, and only shows evidence of evolution when redshifts $z \lesssim 0.4$ are included.[11] This suggests that, at high redshifts, radii even as small as a few tenths of r_{500} could reasonably be used to test the universality of the centre-excluded metallicity. We adopt a radius of $0.3\,r_{500}$ separating the two annuli/shells in our analysis for two reasons. First, the extent of the PSF compared with the cluster means that further reducing the separation radius yields only minor improvements in precision for the outer shell. Secondly, our

[11] Physically, this behaviour likely reflects that the central region where stellar evolution continues to enrich the ICM on average does not correspond to a neat fraction of r_{500}. For this reason, Liu et al. (2020) recently advocated for a more physical core + constant model of the ICM metallicity profile, although constraining this model requires sufficient depth and spatial resolution to measure several metallicity bins per cluster. Here, we continue to use a fraction of r_{500} for simplicity and ease of comparison with previous work.

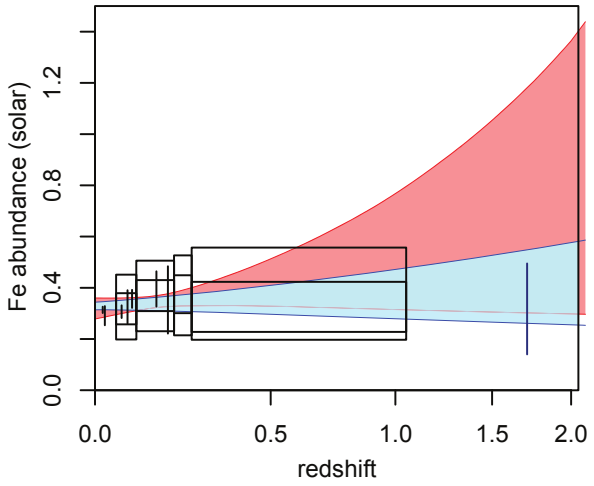

Figure 6. Measured centre-excluded ICM metallicities from *Suzaku* and *Chandra*, and our observations of SPT J0459, and constraints on evolution models. Black points show *Suzaku* measurements of low-redshift clusters (Simionescu et al. 2013; Werner et al. 2013; Urban et al. 2017), while black boxes represent the 68.3 and 95.4 per cent limits from clusters observed by *Chandra* in different redshift ranges (Mantz et al. 2017). Red shading shows the 68.3 per cent confidence limits for power-law models, $\propto (1+z)^{\gamma}$, from these data. The blue point at $z = 1.71$ represents our measurement of SPT J0459, and light blue shading shows the improved model constraints when it is combined with the *Suzaku* and *Chandra* data.

most precise measurement of the centre-excluded metallicity at low redshift comes from Perseus, where a spatially uniform value was measured over 76 regions extending in to $\sim 0.3\,r_{500}$, despite the fact that Perseus, unlike SPT J0459, hosts a well-developed cool core. For completeness, we note that our analysis yields a metallicity of 0.48 ± 0.33 at radii $> 0.5\,r_{500}$ when splitting the data at that larger radius.

Fig. 6 shows the *Suzaku* and *Chandra* data used by Mantz et al. (2017, black points and boxes) and the constraints on evolution models from those data alone (red shading). Here, we have cross-calibrated the *Chandra* data to a normalization determined from *Suzaku*, as described by Mantz et al. (2017), since precise metallicity constraints from *XMM* and *Suzaku* in low-redshift clusters agree well (e.g. Leccardi & Molendi 2008; Urban et al. 2011, 2017; Werner et al. 2013; Simionescu et al. 2015, 2017). To be concrete, the model fitted is a power law, $Z = Z_0(1+z)^{\gamma}$, along with a lognormal intrinsic scatter, $\sigma_{\ln Z}$. When incorporating the centre-excluded metallicity constraint from SPT J0459 at $z = 1.71$ (blue point), we obtain $Z_0 = 0.328 \pm 0.015$, $\sigma_{\ln Z} < 0.06$, and $\gamma = 0.25 \pm 0.34$ (68.3 per cent confidence limits; blue shading in the figure). Thanks to the high precision of the $z \approx 0$ *Suzaku* data, and the high redshift and (relatively) good precision of our measurement for SPT J0459, our constraint on γ is tighter by a factor of ~ 2 compared with those of Ettori et al. (2015) and Mantz et al. (2017). At the same time, there is clearly room for constraints to be improved through new, high-redshift observations, which have disproportionate leverage on the evolution parameter.

5.2 Global scaling relations and evolution

Fig. 7 compares the integrated X-ray luminosity and gas mass (Section 4.2) and average temperature (Section 4.1) for SPT J0459 (collected in Table 3) with two differently selected samples of clusters at lower redshifts. The left column compares with *Chandra* measurements of massive, X-ray selected clusters at $0.0 < z < 0.5$ (median redshift 0.21) from Mantz et al. (2016b), while the right column shows a subset of SPT clusters observed by *XMM* at $0.2 \lesssim z < 1.5$ (median 0.44) from Bulbul et al. (2019). Note that, while there are well-known differences between temperatures measured using *Chandra* and *XMM* in general, we do not expect cross-calibration to be a significant issue for these comparisons, since Bulbul et al. (2019) use only MOS (and not PN) *XMM* data, and the high redshift of SPT J0459 means that our measurements are dominated by soft observer-frame energies where the instrumental response calibrations of the telescopes are in good agreement (as verified in Section 3.2; see also Tsujimoto et al. 2011; Schellenberger et al. 2015). One caveat is that the procedure for determining r_{500} for the purposes of estimating these global properties used here for SPT J0459 is identical to that of Mantz et al. (2016b), but differs from that of Bulbul et al. (2019). We therefore applied a simple adjustment to the $M_{\rm gas}$ value for SPT J0459 in the right column of the figure, accounting for the difference in r_{500} between our determination and that of Bleem et al. (2015), as well as the slope of our measured gas mass profile. This $M_{\rm gas}$ adjustment is an increase of ~ 18 per cent, while any changes to the centrally weighted luminosity and temperature measurements should be negligible in comparison.

Since self-similar evolution in the plotted quantities (Kaiser 1986) is accounted for in Fig. 7, we can (broadly) interpret the presence of SPT J0459 within the distributions of lower redshift clusters as evidence against strong departures from self-similar evolution over the redshift ranges probed (~ 0.2–1.7). This consistency with self-similar evolution is in agreement with the internal constraints on scaling relations from the two comparison samples (Mantz et al. 2016b; McDonald et al. 2017; Bulbul et al. 2019). In comparison with both the X-ray and SZ-selected samples shown, SPT J0459 is perhaps relatively hot for its gas mass and luminosity, but otherwise fairly typical, given a self-similar extrapolation. Note that we would expect this SZ-selected cluster to be relatively hot for its luminosity in comparison with the X-ray-selected sample, due to the dependences of the selection observables on these physical quantities.

6 CONCLUSION

We present results from a very deep *XMM* observation of SPT J0459, the highest (confirmed) redshift SZ-discovered galaxy cluster known. Our data provide a precise constraint on the cluster redshift of $z = 1.705 \pm 0.018$, in agreement with earlier limits from optical and IR photometry. Within $\sim r_{500}$, we measure an emission-weighted temperature of 7.2 ± 0.3 keV and metallicity of $Z/Z_{\odot} = 0.37 \pm 0.08$. Accounting for the *XMM* PSF, we constrain the gas density profile, and use this to estimate the characteristic mass to be $M_{500} = (1.8 \pm 0.2) \times 10^{14}\,M_{\odot}$ – equivalently, $r_{500} = (458 \pm 18)$ kpc – in our reference cosmological model. Comparing the luminosity, temperature, and gas mass of SPT J0459 with lower redshift X-ray and SZ-selected cluster samples, we find broad agreement with self-similarly evolving scaling relations.

For the first time at this high redshift, the data allow us to constrain properties of the intracluster gas in the cluster centre separately from the gas in the outskirts, here defined as $r < 0.3\,r_{500}$ and $r > 0.3\,r_{500}$. In particular, we measure the Fe abundance in the outskirts to be $Z/Z_{\odot} = 0.33 \pm 0.17$, in good agreement with the 'universal' enrichment value of 0.3 measured in the outskirts of nearby clusters. Despite the relatively modest precision of our measurement, the high redshift of this cluster allows us to improve constraints on

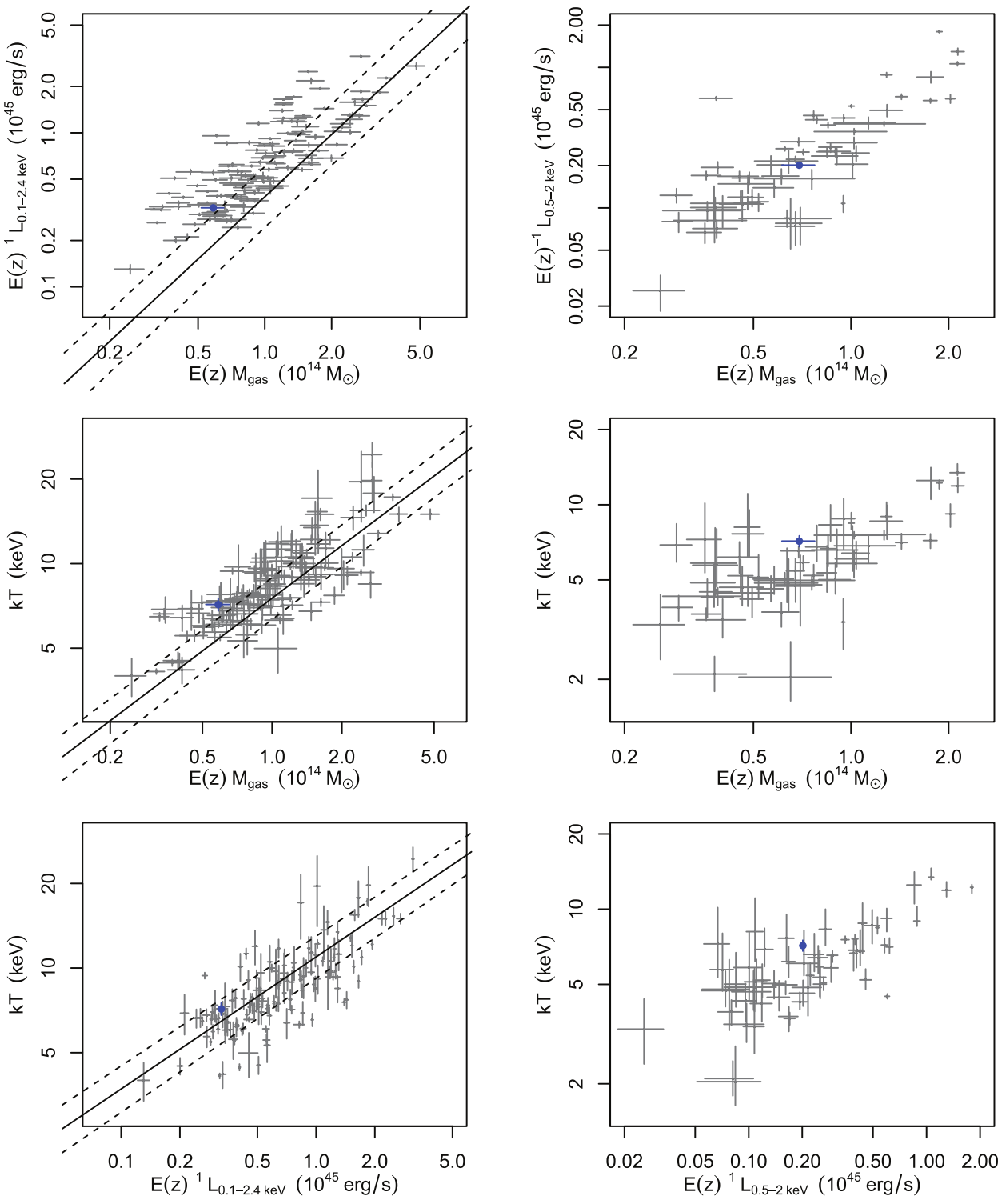

Figure 7. Comparison of the global properties of SPT J0459 (blue point) with lower redshift cluster samples. Factors of $E(z) = H(z)/H_0$ encode self-similar evolution of the scaling relations. Left column: Grey points show measurements from Mantz et al. (2016b, median $z = 0.21$), and solid/dashed lines the corresponding scaling relations (accounting for X-ray flux-selection bias) and their uncertainty (including intrinsic scatter). These measurements were obtained from *Chandra* data, but the procedure for determining each observable (and r_{500}) is essentially the identical to the one used in this work, apart from not needing to model the PSF. Right column: Grey points show measurements of 59 SPT clusters observed by *XMM* (Bulbul et al. 2019; median $z = 0.44$). Here, the gas mass of SPT J0459 has been adjusted for consistency with the method used to determine r_{500} for the other SPT clusters.

power-law metallicity evolution models, $\propto (1+z)^{\gamma}$, by a factor of 2. Combining with lower redshift *Suzaku* and *Chandra* data, we find $\gamma = 0.25 \pm 0.34$, consistent with no evolution in the outskirts metallicity.

That the large-scale metallicity and thermodynamic properties of SPT J0459 appear consistent with the simplest models of cluster formation and evolution reinforces the notion that massive, virialized clusters with deep potential wells represent (relatively)

Table 3. Global properties of SPT J0459. Measurements are within to the characteristic radius r_{500} in three dimensions in the case of mass and gas mass, and in projection for the other quantities. A redshift of $z = 1.71$ is assumed in the derivations of radius, mass, gas mass, and luminosity. The impact of the redshift uncertainty on these quantities is subdominant to statistical uncertainties.

z	r_{500} (kpc)	M_{500} ($10^{14}\,M_{\odot}$)	$M_{\rm gas}$ ($10^{13}\,M_{\odot}$)	kT (keV)	Z ($Z_{\odot}$)	L(0.1–2·4 keV) (10^{44} ergs^{-1})	L(0.5–2·0 keV) (10^{44} ergs^{-1})
1.705 ± 0.018	458 ± 18	1.8 ± 0.2	2.3 ± 0.3	7.2 ± 0.3	0.37 ± 0.08	8.4 ± 0.3	5.20 ± 0.18

physically simple systems once they have formed. This is good news for cluster cosmology tests using current SZ surveys with SPT-3G and Advanced ACT (Benson et al. 2014; Henderson et al. 2016), as well as upcoming SZ and X-ray surveys with the Simons Observatory, CMB-S4 and ATHENA (Nandra et al. 2013; CMB-S4 Collaboration 2016; Cucchetti et al. 2018; Ade et al. 2019), which will find clusters to redshifts $z > 2$. To place these observations on a firm quantitative footing, however, will require dedicated X-ray follow-up of clusters found at these redshifts; for metallicity studies in particular, this requires deeper data than that normally obtained to estimate simple mass proxies. Ultimately, this work at $z > 2$ will benefit from next-generation observatories like ATHENA and *Lynx*, which are planned for launch in the 2030s. In the interim, at slightly lower redshifts, there remains a clear role for deep observations with *XMM*, such as the one used here.

ACKNOWLEDGEMENTS

We thank Stefano Ettori for helpful comments.

We acknowledge support from the National Aeronautics and Space Administration under grant no. 80NSSC18K0578, issued through the *XMM–Newton* Guest Observer Facility; and from the U.S. Department of Energy under contract number DE-AC02-76SF00515.

This work was performed in the context of the South Pole Telescope scientific programme. SPT is supported by the National Science Foundation through grant PLR-1248097. Partial support is also provided by the NSF Physics Frontier Centre grant no. PHY-0114422 to the Kavli Institute of Cosmological Physics at the University of Chicago, the Kavli Foundation and the Gordon and Betty Moore Foundation grant no. GBMF 947 to the University of Chicago. The SPT is also supported by the U.S. Department of Energy. Work at Argonne National Lab is supported by UChicago Argonne LLC, Operator of Argonne National Laboratory (Argonne). Argonne, a U.S. Department of Energy Office of Science Laboratory, is operated under contract no. DE-AC02-06CH11357.

REFERENCES

Adami C. et al., 2018, A&A, 620, A5
Ade P. et al., 2019, J. Cosmol. Astropart. Phys., 2019, 056
Allen S. W., Fabian A. C., 1998, MNRAS, 297, L63
Allen S. W., Evrard A. E., Mantz A. B., 2011, ARA&A, 49, 409
Anderson M. E., Bregman J. N., Butler S. C., Mullis C. R., 2009, ApJ, 698, 317
Andreon S., 2012, A&A, 546, A6
Andreon S., Newman A. B., Trinchieri G., Raichoor A., Ellis R. S., Treu T., 2014, A&A, 565, A120
Arnaud K. A., 1996, in Jacoby G. H., Barnes J., eds, ASP Conf. Ser. Vol. 101, Astronomical Data Analysis Software and Systems V. Astron. Soc. Pac., San Francisco, p. 17
Asplund M., Grevesse N., Sauval A. J., Scott P., 2009, ARA&A, 47, 481
Baldi A., Ettori S., Molendi S., Balestra I., Gastaldello F., Tozzi P., 2012, A&A, 537, A142
Balestra I., Tozzi P., Ettori S., Rosati P., Borgani S., Mainieri V., Norman C., Viola M., 2007, A&A, 462, 429
Balucinska-Church M., McCammon D., 1992, ApJ, 400, 699
Barnes D. J., Kay S. T., Henson M. A., McCarthy I. G., Schaye J., Jenkins A., 2017, MNRAS, 465, 213
Battaglia N., Bond J. R., Pfrommer C., Sievers J. L., 2013, ApJ, 777, 123
Benson B. A. et al., 2014, Millimeter, Submillimeter, and Far-Infrared Detectors and Instrumentation for Astronomy VII. p. 91531P (arXiv: 1407.2973)
Biffi V. et al., 2017, MNRAS, 468, 531
Bleem L. E. et al., 2015, ApJS, 216, 27
Böhringer H. et al., 2004, A&A, 425, 367
Brodwin M., McDonald M., Gonzalez A. H., Stanford S. A., Eisenhardt P. R., Stern D., Zeimann G. R., 2016, ApJ, 817, 122
Bulbul E. et al., 2019, ApJ, 871, 50
Cash W., 1979, ApJ, 228, 939
CMB-S4 Collaboration, 2016, preprint (arXiv:1610.02743)
Cucchetti E. et al., 2018, A&A, 620, A173
De Grandi S., Ettori S., Longhetti M., Molendi S., 2004, A&A, 419, 7
de Haan T. et al., 2016, ApJ, 832, 95
Ebeling H., Edge A. C., Allen S. W., Crawford C. S., Fabian A. C., Huchra J. P., 2000, MNRAS, 318, 333
Ebeling H., Edge A. C., Henry J. P., 2001, ApJ, 553, 668
Eke V. R., Navarro J. F., Frenk C. S., 1998, ApJ, 503, 569
Ettori S., Baldi A., Balestra I., Gastaldello F., Molendi S., Tozzi P., 2015, A&A, 578, A46
Fabjan D., Borgani S., Tornatore L., Saro A., Murante G., Dolag K., 2010, MNRAS, 401, 1670
Giodini S., Lovisari L., Pointecouteau E., Ettori S., Reiprich T. H., Hoekstra H., 2013, Space Sci. Rev., 177, 247
Gobat R. et al., 2011, A&A, 526, A133
Gobat R. et al., 2019, A&A, 629, A104
Gonzalez A. H. et al., 2019, ApJS, 240, 33
Hasselfield M. et al., 2013, J. Cosmol. Astropart. Phys., 7, 8
Henderson S. W. et al., 2016, J. Low Temp. Phys., 184, 772
HI4PI Collaboration, 2016, A&A, 594, A116
Kaiser N., 1986, MNRAS, 222, 323
Kalberla P. M. W., Burton W. B., Hartmann D., Arnal E. M., Bajaja E., Morras R., Pöppel W. G. L., 2005, A&A, 440, 775
Leccardi A., Molendi S., 2008, A&A, 487, 461
Liu A., Tozzi P., Ettori S., De Grand i S., Gastaldello F., Rosati P., Norman C., 2020, A&A, 637, A58
Mantz A. B. et al., 2014, ApJ, 794, 157
Mantz A. B. et al., 2016b, MNRAS, 463, 3582
Mantz A. B. et al., 2018, A&A, 620, A2
Mantz A. B., Allen S. W., Morris R. G., Schmidt R. W., von der Linden A., Urban O., 2015, MNRAS, 449, 199
Mantz A. B., Allen S. W., Morris R. G., Schmidt R. W., 2016a, MNRAS, 456, 4020
Mantz A. B., Allen S. W., Morris R. G., Simionescu A., Urban O., Werner N., Zhuravleva I., 2017, MNRAS, 472, 2877
Maughan B. J., Jones C., Forman W., Van Speybroeck L., 2008, ApJS, 174, 117
McDonald M. et al., 2016, ApJ, 826, 124
McDonald M. et al., 2017, ApJ, 843, 28
Mernier F. et al., 2017, A&A, 603, A80
Nagai D., Vikhlinin A., Kravtsov A. V., 2007, ApJ, 655, 98
Nandra K. et al., 2013, preprint (arXiv:1306.2307)

Planck Collaboration, 2016, A&A, 594, A27
Planelles S., Borgani S., Dolag K., Ettori S., Fabjan D., Murante G., Tornatore L., 2013, MNRAS, 431, 1487
Read A. M., Rosen S. R., Saxton R. D., Ramirez J., 2011, A&A, 534, A34
Rykoff E. S. et al., 2012, ApJ, 746, 178
Salvetti D. et al., 2017, Exp. Astron., 44, 309
Schellenberger G., Reiprich T. H., Lovisari L., Nevalainen J., David L., 2015, A&A, 575, A30
Simionescu A. et al., 2013, ApJ, 775, 4
Simionescu A., Werner N., Urban O., Allen S. W., Ichinohe Y., Zhuravleva I., 2015, ApJ, 811, L25
Simionescu A., Werner N., Mantz A., Allen S. W., Urban O., 2017, MNRAS, 469, 1476
Singh P., Saro A., Costanzi M., Dolag K., 2020, MNRAS, 494, 3728
Snowden S. L., Mushotzky R. F., Kuntz K. D., Davis D. S., 2008, A&A, 478, 615
Strazzullo V. et al., 2019, A&A, 622, A117
Thölken S., Lovisari L., Reiprich T. H., Hasenbusch J., 2016, A&A, 592, A37
Tsujimoto M. et al., 2011, A&A, 525, A25
Urban O., Werner N., Simionescu A., Allen S. W., Böhringer H., 2011, MNRAS, 414, 2101
Urban O., Werner N., Allen S. W., Simionescu A., Mantz A., 2017, MNRAS, 470, 4583
Urdampilleta I., Mernier F., Kaastra J. S., Simionescu A., de Plaa J., Kara S., Ercan E. N., 2019, A&A, 629, A31
Werner N., Urban O., Simionescu A., Allen S. W., 2013, Nature, 502, 656
Willis J. P. et al., 2013, MNRAS, 430, 134
Willis J. P. et al., 2020, Nature, 577, 39

This paper has been typeset from a TEX/LATEX file prepared by the author.